Anisotropy at twin interfaces in RT_{12} (R = rare earth; T = transition metal) magnets

Christopher E. Patrick *

Department of Materials, University of Oxford, Parks Road, Oxford OX1 3PH, United Kingdom

(Received 12 May 2025; revised 6 August 2025; accepted 8 August 2025; published 22 August 2025)

RT_{12} materials continue to attract attention due to their potential use as "rare-earth-lean" permanent magnets, but converting their promising intrinsic properties into practical high performance remains an elusive goal. Sophisticated experimental characterization techniques are providing unprecedented insight into the structure of these materials at the atomistic scale. Atomistic spin dynamics or micromagnetics simulations could help unravel the links between these structures and resultant magnet performance, but require input data describing the intrinsic magnetic properties. Here, first-principles calculations based on density functional theory are used to determine these properties for two model interface structures which have been derived from recently reported high-resolution electron microscopy images. One model structure is a stoichiometric twin formed by mirroring the RT_{12} structure in the (101) plane, and the other model structure is a "stacking fault" involving the insertion of a RT_4 plane and a displacement along the [100] axis. Magnetic moments and crystal field coefficients have been calculated for the optimized structures. The interfaces modify the magnetic properties at the sub-nm scale. In particular, in the R-rich region of the "stacking fault," the local easy axis of magnetization rotates by 49° from its bulk direction, which may lead to reduced coercivity through the easier nucleation of reverse domains.

DOI: 10.1103/syc2-qzdf

I. INTRODUCTION

The need for permanent magnets with a reduced rare-earth content compared to widely used Nd-Fe-B and Sm-Co continues to drive research into "one-twelve" materials with formula RT_{12}, where R is a rare-earth element and T is a transition metal [1,2]. Alloys of $SmFe_{12}$ have intrinsic properties which satisfy the key requirements of a permanent magnet, namely, a large volume magnetization, a high Curie temperature, and a strong uniaxial magnetocrystalline anisotropy [3–5]. Pure $SmFe_{12}$ is thermodynamically unstable, but stable alloys can be formed through partial substitution of Fe with transition metals such as Ti and V, or of Sm with elements such as Zr, Gd, or Y [6–14]. Optimizing the composition requires considering both performance and cost. For instance, Co is an excellent substitute for Fe from the point of view of magnetic properties, but suffers from similar supply issues as the rare earths themselves [15].

Aside from cost, the outstanding challenge surrounding one-twelve materials is how to convert promising intrinsic behavior into the key extrinsic properties of remanence and coercivity [16–21]. For these properties, the microstructure of the materials is crucial, which creates the need to characterize and understand the role of secondary phases and defects. There has been particular interest in the presence of twins in one-twelve samples, with boundary regions proposed to act as nucleation sites for magnetization reversal [22–25]. Recently, high-resolution high-angle annular dark-field images obtained from scanning tunneling electron microscopy (HAADF-STEM) showed twin boundaries at an unprecedented level of detail [26]. In that work, two markedly different HAADF-STEM images were observed depending on the composition of the RT_{12} alloy. Atomistic models of these interfaces (as proposed in the current work) are shown in Fig. 1. The original images appear as Fig. 3 in Ref. [26].

This ability to visualize the structure of interfaces at the atomistic scale raises two key questions: (i) How does the modified atomistic structure affect the magnetic properties of atoms in this region, and (ii) what impact do these modified magnetic properties have on the material's macroscopic performance as a permanent magnet? Considering the first question, the local environment (crystal field) of R atoms is responsible for their large magnetocrystalline anisotropy [27], so any significant perturbation to the crystal field should affect the anisotropy. For instance, calculations of the crystal field of a $Nd_2Fe_{14}B$ slab found that Nd atoms at the (001) surface had easy-plane rather than easy-axis anisotropy [28]. We may also expect modification of the magnetic moments of the atoms and of the exchange coupling between them, as has also been shown for Nd-Fe-B interfaces [29].

Considering the second question regarding the impact on permanent magnet performance, inhomogeneities in the anisotropy form the basis of Kronmüller's theory of why the (extrinsic) coercive field is only a fraction of the (intrinsic) anisotropy field, due to the smaller nucleation fields of reverse domains in regions of low anisotropy [30]. Analytical calculations also show how inhomogeneous anisotropy leads to pinning of domain walls, which is the relevant coercivity mechanism for Sm-Co magnets [31]. Advances in the computational modeling of micromagnetics (MM)

*Contact author: christopher.patrick@materials.ox.ac.uk

Published by the American Physical Society under the terms of the Creative Commons Attribution 4.0 International license. Further distribution of this work must maintain attribution to the author(s) and the published article's title, journal citation, and DOI.

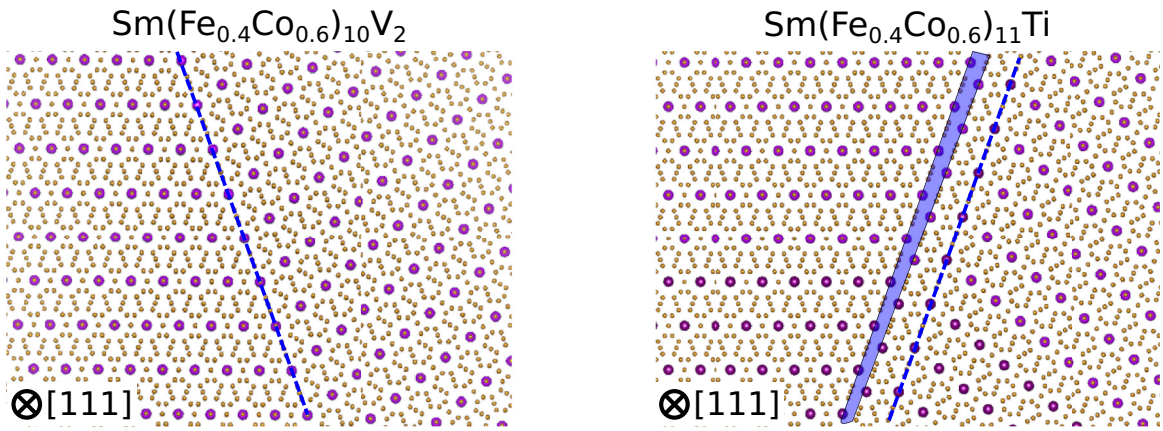


FIG. 1. Representations of the two atomistic models proposed in the current work which reproduce the HAADF-STEM images shown in Fig. 3 of Ref. [26]. The structures are viewed along the [$\bar{1}$11] direction, which lies in the (101) twin plane. *R* and *T* atoms are represented as large pink or small yellow circles, respectively. The schematics of these structures are shown in Fig. 2.

[32] and atomistic spin dynamics (ASD) [33] have enabled numerical simulations at a higher level of complexity than possible with analytical calculations, to gain material-specific insight into magnetization reversal and coercivity. Some examples are calculating domain-wall widths in bulk $Nd_2Fe_{14}B$ [34,35], domain-wall structures in Sm_2Co_{17} [36], and nucleation/coercive fields in various materials, including RT_{12} magnets [24,37–39].

Both MM and ASD allow the researcher to specify a material's microscopic properties and then carry out numerical "measurements" of macroscopic magnetic performance. The ability of such simulations to obtain realistic outputs is determined by the accuracy of the equations which make up the model and by the quality of the input data. The required input data are the intrinsic properties of magnetization, exchange, and anisotropy, resolved at the atomistic/submicron level for ASD/MM, respectively. When simulating a material composed of well-characterized phases, these intrinsic properties might be derived from experimental measurements on single crystals of the relevant phases. However, the interfaces regions shown in Fig. 1 are not crystalline and the environments of the atoms in the sub-nm interfacial regions do not resemble bulk phases. Determining the magnetic properties of these specific atoms is therefore a formidable experimental challenge.

First-principles calculations provide an attractive alternative method of obtaining the intrinsic properties of novel structures. The sub-nm length scale is ideally suited to calculations based on (spin) density functional theory (DFT) [40,41]. Solving the fundamental equations of DFT, including using the Hellman-Feynman theorem to obtain forces on atoms, allows the first-principles calculation of structural parameters (e.g., bond lengths), and properties deriving from electrons such as magnetic moments and the crystal field. Crucially, DFT does not require prior empirical knowledge of the system under study, only the approximate positions and types of the atoms involved. In this work, this information is deduced from the HAADF-STEM images. The principal complication associated with DFT calculations on rare-earth magnets is modeling of exchange and correlation, with the most widely used approaches based on the local density or generalized gradient approximations struggling to describe the lanthanide-4f electrons [42]. However, a number of methods have been developed to overcome this issue and are in active use, such as the open-core approach, DFT+U, the self-interaction correction, and dynamical mean-field theory [43–49]. In this work, the "yttrium-analog" (Y-analog) approach is employed, where all calculations are performed with Y as the rare-earth element [50]. The justification for this approach is that it is the valence electrons which have the greatest effect on the transition-metal magnetism and the crystal field [51]. Since Y^{3+} and Sm^{3+} have the same s^2d valence electronic structure, Y is a convenient analog, free of 4f electrons, to investigate these properties. The Y-analog approach was inspired by experimental literature, where studies on materials such as $Y_2Fe_{14}B$ [52], YCo_5 [53], and $YFe_{11}Ti$ [54] provided valuable insight into their lanthanide-based counterparts.

The purpose of this study is to use first-principles calculations to obtain the magnetic properties of atoms in the twin boundary interface regions recently observed in one-twelve materials, thus addressing the first key question posed above. The HAADF-STEM images from Ref. [26] are used to derive atomistic models of the interfaces. Applying DFT to these models yields optimized structures and local magnetic moments. The crystal field at each *R* site in the interface models is then calculated within the Y-analog approach. Crystal field theory allows the single-ion anisotropy energy for Sm-based magnets to be deduced, giving local anisotropy energies and magnetization directions. The calculations show that there are changes to the magnetic moments and crystal field only within a few Å of the interface. However, this change in crystal field is substantial for one of the structures, resulting in a rotation of the easy direction by 49° away from the *c* axis.

The rest of this manuscript is ordered as follows. Section II describes the construction of the interface models in Fig. 1 and their relation to the RT_{12} structure. Section II also describes the embedding of these structures in periodically repeating simulation cells and gives the methodological details of the DFT calculations, including an overview of the method of calculating the crystal field coefficients. Section III presents the results of the calculations, including radial distribution

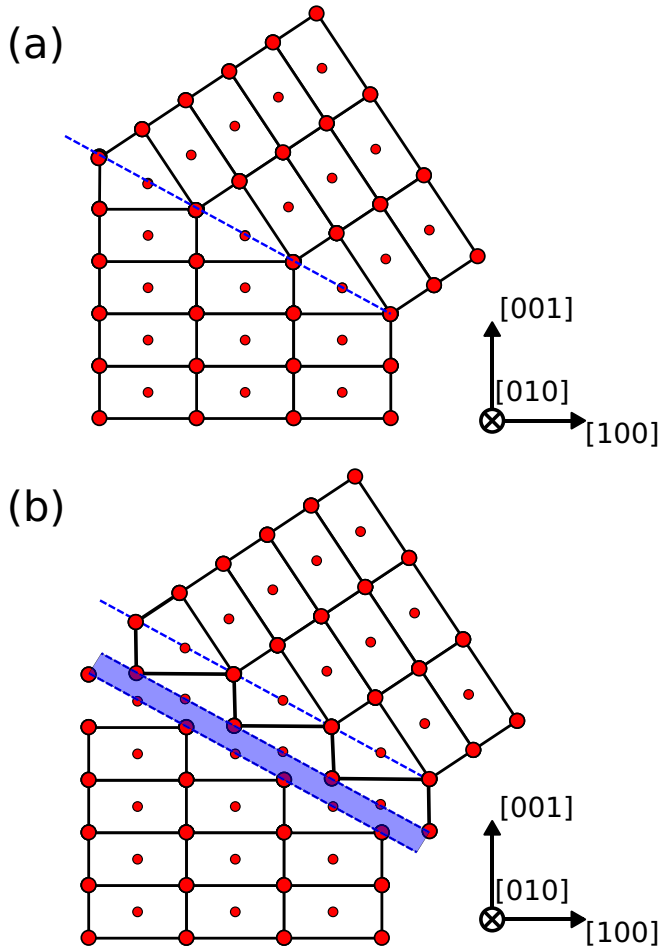


FIG. 2. The same structures as shown in Fig. 1 of (a) $Sm(Fe_{0.4}Co_{0.6})_{10}V_2$ and (b) $Sm(Fe_{0.4}Co_{0.6})_{11}Ti$, viewed along the [010] direction, with only R sites shown; the larger and smaller circles correspond to the sites at the corners and center of the bct cell, respectively. The (101) twin plane is shown as the blue dashed line. Panel (b) also shows, as a blue-shaded rectangle, the extended defect formed by the cleaving, displacement, and insertion of an RT_4 plane. Note that the axes refer to the lowest region in the figures.

functions of the relaxed structures, magnetic moments, and crystal field coefficients. The crystal field coefficients are used to construct the single-ion anisotropy energy in a classical approximation. Finally, Sec. IV presents conclusions and identifies areas for future study.

II. METHODOLOGY

A. Models of extended interface structures

Figure 3 of Ref. [26] reported HAADF-STEM images of two different structures, both formed from twinning along {101} planes, observed for $Sm(Fe_{0.4}Co_{0.6})_{10}V_2$ and $Sm(Fe_{0.4}Co_{0.6})_{11}Ti$. Figure 1 of the current work proposes atomistic structures of the interfaces, based on these images. The orientations in Fig. 1 have been chosen to match the images in Ref. [26], but Fig. 2 gives a schematic view of the same structures which better illustrates how the models were constructed. RT_{12} has a body-centered-tetragonal (bct) structure, with $a > c$. The rare-earth atoms occupy the (0,0,0) and $(\frac{1}{2}, \frac{1}{2}, \frac{1}{2})$ positions and, for simplicity, we only show these positions in Fig. 2. The (101) plane which bisects the conventional cell contains R and T atoms at a ratio of RT_4, with the T atoms equally distributed on $8i$ and $8f$ Wyckoff sites. The $Sm(Fe_{0.4}Co_{0.6})_{10}V_2$ structure [Fig. 2(a)] is formed simply by reflecting the crystal in this plane. This operation does not affect the 1:12 stoichiometry. The more complicated $Sm(Fe_{0.4}Co_{0.6})_{11}Ti$ structure also has this reflection. In addition, there is an extended defect which, as shown in Fig. 2(b), is formed by cleaving the crystal along the (101) plane and introducing a displacement between the cleaved sections of $a/2$ in the [100] direction. In addition, an RT_4 plane of atoms is introduced into the created gap. These additional atoms result in a local stoichiometry which is R-rich compared to the RT_{12} bulk. Note that the same defect can be described equivalently as a removal of all T atoms lying between a pair of adjacent (101) planes followed by the introduction of a displacement of $a/2$ along $[\bar{1}00]$ between the regions. In the $Sm(Fe_{0.4}Co_{0.6})_{11}Ti$ structure, this defect is followed by a reflection in the next (101) plane [Fig. 2(b)]. These models provide an excellent account of the experimentally observed images in Fig. 3 of Ref. [26].

B. Periodic models for first-principles calculations

The extended interface structures shown in Figs. 1 and 2 break translational symmetry. However, many implementations of first-principles electronic structure theories assume periodically repeating simulation cells, which allow efficient and well-converged solutions of the numerical equations through the use of Bloch's theorem and plane-wave basis sets [55]. It is therefore desirable to construct models which reproduce the relevant atomic environments of Fig. 1, but also have periodically repeating simulation cells. These models are shown in Fig. 3 and are labeled as "twin" (T) or "stacking fault" (SF) [56]. The model T reproduces the stochiometric (101) twinning seen in both interface structures (blue lines in Figs. 1 and 2). The model SF reproduces the motif seen in the $Sm(Fe_{0.4}Co_{0.6})_{11}Ti$ structure, whereby an offset is introduced between adjacent (101) planes and the local stoichiometry becomes R-rich (shaded region of Figs. 1 and 2). These models were constructed first by noting that the translational symmetry parallel to the (101) plane is not broken by the interface, so for both models, one can choose two of the three simulation cell vectors to also lie in this plane, with minimal, equal lengths of $\sqrt{(2a^2 + c^2)}/2$. The third simulation cell vector is different for the two models. For model T, it is perpendicular to the (101) plane and translational symmetry is achieved by having two twin planes per simulation cell, located at the center and the edges of the blue rectangle in Fig. 3. For model SF, the third vector is not perpendicular to the (101) plane, but instead chosen to reproduce the stacking fault with pairs of R atoms at the cell edge located at a distance $a/2$ from each other. The remaining choice is how large to make the simulation cell, i.e., how many RT_4 planes should be included. A larger number better represents the true, aperiodic interface, but increases the computational expense. The models in Fig. 3 were chosen to have similar distances (∼20 Å) between

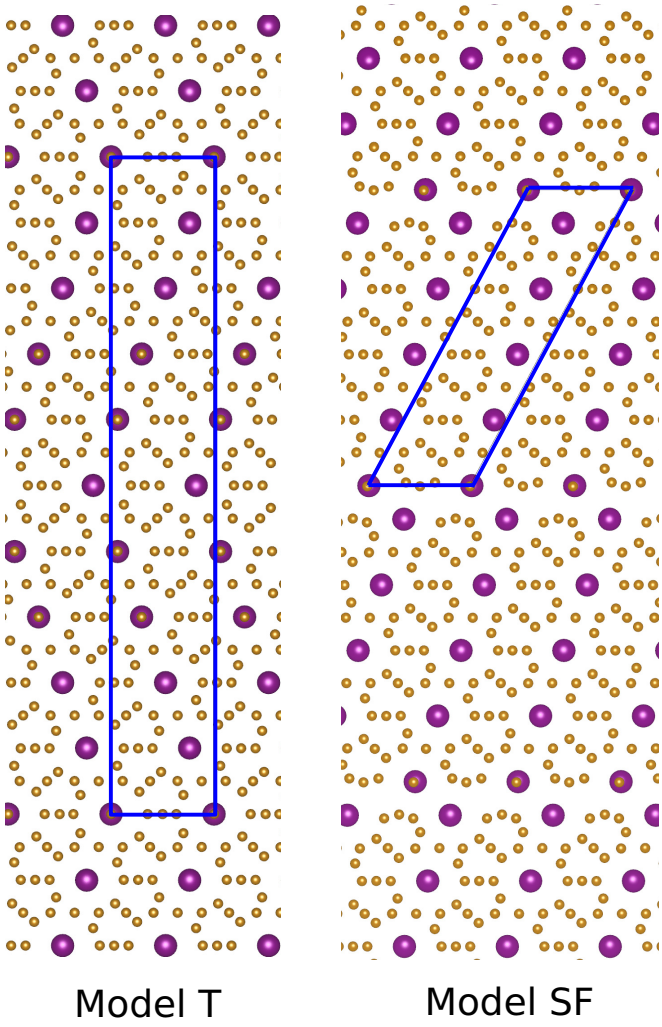


FIG. 3. The two periodically repeating models used in this work. The models are viewed along [$\bar{1}$11], which coincides with the direction of one of the cell vectors. The boundary of the unit cell in the perpendicular plane is shown in blue. These models were structurally relaxed as described in the text. Note that the R atoms do not all lie in the plane of the page. The perpendicular distance between repeated interface planes is 20.5 Å for model T and 18.5 Å for model SF.

repeated interface planes. This distance is justified by the results presented later in the manuscript, where it is shown that the interface's influence (e.g., on local magnetic moments or the anisotropy) has a much shorter range. The cell vectors and atomic positions are supplied as Supplemental Material [57].

C. The Y-analog approach and choice of T

As noted in Sec. I, a huge variety of RT_{12} alloys can be formed through substitution of R and/or T. All of the calculations presented in this work are carried out on a single composition, which is YFe_{12}. The use of Y as the rare-earth element is the central idea of the Y-analog approach [50]. Its justification is that it is the valence electronic structure—the $6s^2 5d$ electrons for the lanthanides ($5s^2 4d$ for Y)—which hybridizes with transition-metal electrons, setting up the (antiferromagnetic) exchange coupling and the crystal field [43,50]. In this picture, the lanthanide $4f$ shell is anchored to the valence electronic structure through the on-site $4f$-$5d$ interaction, but the $4f$ electrons themselves do not influence the electronic structure. This is an approximation, and calculations that take the $4f$ electrons into account do show differences with the Y-analog model, for instance, in calculating variations in Curie temperatures [48] or higher-order crystal field coefficients [58]. However, for the lower-order crystal field coefficients (which tend to dominate magnetic behavior at working temperatures) and to obtain a general picture of the magnetic properties, the Y-analog model is an attractive choice. It provides a similar accuracy to the open-core method [50], but circumvents any complications from simulating lanthanide elements in DFT. Furthermore, the method is numerically robust thanks to the use of plane-wave basis sets.

For the transition metal, this work focuses exclusively on T = Fe and does not take into account any specific effects of the alloying elements. Energy-dispersive spectroscopy (STEM-EDS) can be used to distinguish between R and T sites in the HAADF-STEM images in Ref. [26], but not to identify individual Fe/Co/Ti/V sites. Calculations on bulk RT_{12} have been used to identify preferred sites of low concentrations of dopants, e.g., Refs. [13,14], and, in principle, a similar analysis could be carried out for the interface models in Fig. 3. However, a comprehensive exploration of the configuration space of the (Fe,Co,Ti/V) alloy, particularly one which is free from the finite-size effects associated with periodically repeating simulation cells, would be a significant computational undertaking and beyond the scope of the current investigation. Such an exploration is therefore reserved for future work, which should also aim to elucidate the relationship between a sample's composition and the likelihood that it will form a particular interface structure.

Whilst focusing on a single T element may seem like a limitation, recent work has highlighted the importance of studying the crystal field of the $R\mathrm{Fe}_{12}$ host. Reference [59] demonstrated how the modification to the crystal field due to Ti substitutions in bulk $R\mathrm{Fe}_{12}$ could be well described by a point charge model (PCM) [59]. Test calculations associated with that work showed how Co substitutions did not strongly affect the crystal field, which is expected from the PCM due to the similar atomic numbers of Co and Fe. However, for Ti or V substitution, the effects can be significant. Taking the crystal field of the unperturbed $R\mathrm{Fe}_{12}$ host calculated in the current work, and applying the methodology of Ref. [59], will allow the single-ion anisotropy to be calculated for arbitrary distributions of substituting atoms. As noted in Sec. I, these anisotropy energies are essential input data for larger-scale ASD or MM simulations.

D. Model construction and relaxation

The models in Fig. 3 were constructed using RT_{12} lattice constants of $a = 8.497$ Å and $c = 4.687$ Å, which were previously calculated using DFT for SmFe_{12} in Ref. [60]. The simulation cell vectors were fixed according to these values and the positions of all atoms in the cell were relaxed until the force on each atom was below 0.05 eVÅ^{-1}. The same approach was used for bulk calculations which were

also carried out for comparison. The decision to fix lattice vectors while allowing atomic positions to relax was taken in order to match as closely possible previous uses of the Y-analog model and ensure that there were no net forces on atoms in the unit cell (although an overall strain will still be present due to the differing lattice constants of YFe_{12} and $SmFe_{12}$). The calculations used the local-density approximation to exchange and correlation [61], and treated the core-valence interaction using the projector-augmented wave (PAW) method [62], as implemented in the GPAW code [63]. The electronic wave functions were expanded in a plane-wave basis setup to a maximum cutoff energy of 800 eV, and reciprocal space was sampled using nonshifted grids of size $4 \times 4 \times 1$ for model T, $4 \times 4 \times 2$ for model SF, and $4 \times 4 \times 6$ for bulk. The electronic states were occupied according to the Fermi-Dirac distribution with width 0.01 eV.

E. Crystal field calculations

Crystal field coefficients were calculated using the methodology described in Ref. [50]. In this approach, the DFT Kohn-Sham potential $V(\mathbf{r})$ (which includes both electrostatic interactions and exchange and correlation [41]) is used to calculate the crystal field coefficients B_{lm}, through the equation

$$B_{lm} = \left(\frac{2l+1}{4\pi}\right)^{\frac{1}{2}} \int_0^{r_c} r^2 n^0_{4f}(r) V_{lm}(r) dr.$$

In this equation, $n^0_{4f}(r)$ is the normalized $4f$ electron charge density, which is obtained in a separate calculation on bulk $SmFe_{12}$ using the self-interaction correction [64]. $V_{lm}(r)$ is obtained from an angular decomposition of the Kohn-Sham potential using the complex spherical harmonics, $V(\mathbf{r}) = \sum_{lm} V_{lm}(r) Y_{lm}(\theta, \phi)$. Reference [50] describes the conversion of the Kohn-Sham potential from a plane-wave representation to that on a radial grid, including the appropriate PAW corrections. The radial limit r_c of the integrals was chosen to be 1.65 Å, similar to Ref. [50]. Convergence checks were carried out to ensure that the computational parameters described in Sec. II D were also sufficiently accurate to calculate crystal field coefficients. Also, since the Kohn-Sham potential depends on spin through the exchange and correlation terms, the method generates separate crystal field coefficients for spin-up and spin-down electrons. Here, the differences between the two sets are small, and therefore the presented results are averages over the spin directions. Finally, the calculated coefficients B_{lm} are related to the conventional representation through $A_{lm}\langle r^l \rangle = \alpha_{lm} B_{lm}$, where the prefactors α_{lm} are tabulated in Ref. [65].

III. RESULTS AND DISCUSSION

A. Structural relaxation

Figure 3 shows the structurally relaxed interface models. The only atoms whose positions noticeably change during the structural relaxation are those located directly at the interface in model SF, in the adjacent YFe_4 planes. As can be seen by comparing with any of the other YFe_4 planes in Fig. 3, these Fe atoms are displaced from the (101) plane. Further analysis of the structure can be carried out using radial distribution functions (RDFs). Figure 4 shows the RDFs for Y atoms located directly at the interface for each model, compared to the RDF for the bulk structure. The bulk and model T RDFs are indistinguishable from each other. This emphasizes that the mirror operation shown in Fig. 2(a) affects the orientation of the symmetry axis, but does not introduce new atoms. However, the RDFs calculated for model SF show that the local environment of Y atoms at the interface is Y-rich compared to bulk. In the unrelaxed structure, one of the two Y atoms which are located at a distance of 4.69 Å ($= c$) in bulk is brought closer, to a distance of 4.25 Å ($= a/2$). Furthermore, two new Y atoms are introduced at a distance of 4.85 Å $[= \sqrt{(a^2 + c^2)}/2]$. After relaxation, the nearest Y-Y distance reduces from 4.25 Å to 3.90 Å, while the distance to the two new Y atoms increases from 4.85 Å to 4.99 Å. Therefore, a Y atom at the interface in model SF is surrounded by four other Y atoms within a radius of 5 Å, compared to bulk or model T where there are only two. Furthermore, in model SF, there are two fewer Fe atoms in the first coordination shell (18) compared to bulk or model T (20).

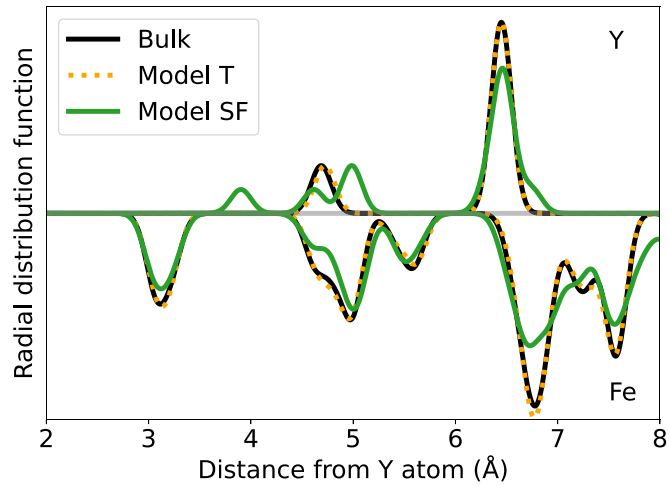


FIG. 4. RDFs for the Y atoms located directly at the interface in model T or model SF, and for an Y atom in bulk YFe_{12}. The positive or negative scale describes distances to Y or Fe atoms, respectively. These RDFs correspond to structures which were relaxed, as described in Sec. II D.

B. Magnetic moments

Figure 5 shows the magnetic moments of the Fe atoms in the relaxed interface models. The local moment size is most strongly affected by whether the atom sits at the crystallographic $8i$, $8j$, or $8f$ position. For either model, all atoms at a distance greater than 4 Å from the interface deviate by less than $0.03\mu_B$ from their bulk values. Indeed, for model T, all local moments are within $0.1\mu_B$ of their bulk values, even the $8i$ and $8f$ atoms located directly in the mirror plane. Therefore, just as Fig. 4 emphasized the similarity between model T and the bulk in terms of atomistic structure, Fig. 5 demonstrates this similarity in terms of electronic structure. However, in model SF, the Fe atoms that are closest to the interface do show stronger deviations, particularly the four $8f$ atoms located 1.0 Å from the interface. These atoms have

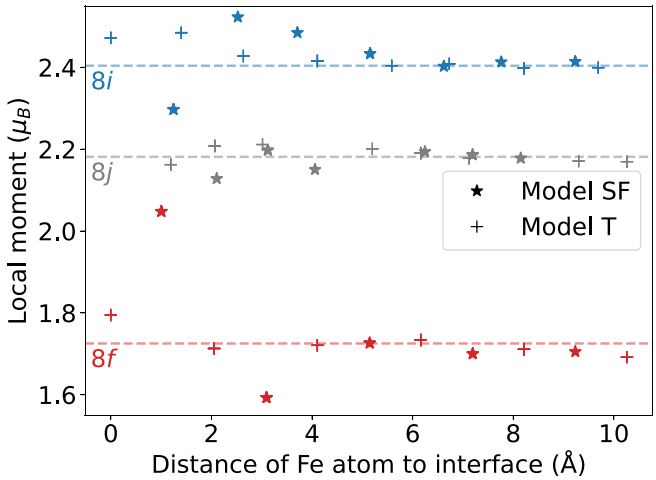


FIG. 5. Local magnetic moments of Fe atoms for the interface models (symbols), compared to bulk (horizontal dashed lines). Blue/gray/red corresponds to crystallographic $8i/8j/8f$ positions. Note that zero distance corresponds to the reflection plane in model T, while for model SF, it is the plane directly between adjacent RT_4 planes (which contains no atoms).

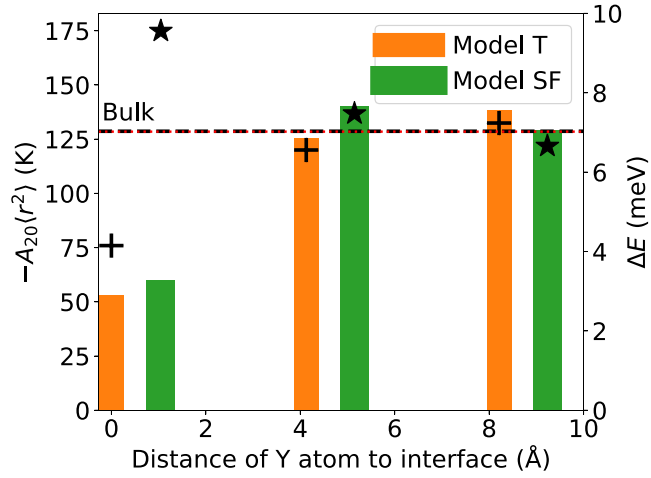


FIG. 6. $A_{20}\langle r^2\rangle$ crystal field coefficients (bars, left axis) and classical anisotropy energy ΔE (symbols, right axis) for the different interface models. Bulk values are shown as horizontal lines.

moments of $2.05\mu_B$, an enhancement of $0.33\mu_B$ compared to bulk. The local moments of the Y atoms show much smaller deviations from their bulk value, of the order of $0.01\mu_B$.

C. Crystal field coefficients

In bulk YFe_{12}, there is one unique Y site and its high symmetry leads to nonzero crystal field (CF) coefficients $A_{lm}\langle r\rangle^l$ only for (l, m) equal to (2,0), (4,0), (4, ±4), (6,0), and (6, ±4). However, the lower symmetry of the interface models means that there are three distinct Y sites in both model T and model SF, as can be deduced by inspecting Fig. 3. There are also no restrictions on the (l, m) values which result in nonzero CF coefficients. Therefore, CF coefficients were calculated for all possible m values when $l = 2, 4, 6$. It should be noted that CF coefficients depend on the coordinate frame used to calculate them. Here, the necessary rotations were applied so that both models and the bulk structure shared a common reference frame.

Figure 6 shows the (negative) values of $A_{20}\langle r\rangle^2$ for the different Y sites in the models, as a function of distance from the interface plane. $-A_{20}\langle r\rangle^2$ is often the focus of analysis since, under certain conditions and approximations, it is proportional to the conventional anisotropy constant [49]. The value of 129 K calculated for bulk YFe_{12} is shown as a dashed line in Fig. 6. The first important feature in Fig. 6 is that the R sites located away from the interface plane, at a distance greater than 4 Å, have very similar CF values to bulk. This is true for all (l, m) values considered, not just (2,0). This mirrors behavior found previously [59], where the perturbation to the crystal field due to the introduction of point defects had a limited range (again, 4 Å).

However, the magnitude of $A_{20}\langle r\rangle^2$ is significantly reduced for the R sites closest to the interface plane. It is important to realize that this does not necessarily mean that the single-ion anisotropy energy at these sites is smaller than in bulk, since this quantity is affected by all (l, m) coefficients, not just (2,0). However, the reduced magnitude of $A_{20}\langle r\rangle^2$ does show that the magnetization is less inclined to point along the c-axis direction. This behavior is not surprising, particularly for model T, where sites at the twin plane have two possible c axes to choose from (one for each grain) and there is no reason to favor one above the other. Indeed, calculations below find that the easy direction at this site points along the average of the c axes of the individual grains.

D. Classical anisotropy energy and easy directions

The behavior of $A_{20}\langle r\rangle^2$ in Fig. 6 and of the other CF coefficients (not shown) leads to the conclusion that only the atoms in the immediate vicinity of the interface structures in Fig. 1 have strongly modified crystal fields. In order to evaluate the effect on the anisotropy energy, the calculated CF coefficients could be fed into the "standard model" spin Hamiltonian for rare-earth magnets to obtain the energy level splitting [66]. However, since this Hamiltonian also involves the exchange field generated by the transition metal, it would be difficult to isolate the contribution of the modified crystal field. Instead, the CF coefficients here are used to construct the classical single-ion anisotropy energy $E(\theta, \phi)$, through [59]

$$E(\theta,\phi) = \sum_{lm} \mathcal{A}_l B_{lm}\, d_l^{0m}(\theta) e^{im\phi}$$
$$= \sqrt{\frac{4\pi}{2l+1}} \sum_{lm} \mathcal{A}_l B_{lm} Y_{lm}(\theta,\phi). \quad (1)$$

The angles (θ, ϕ) describe the orientation of the local magnetic moment at that site. The prefactor $\mathcal{A}_l$ depends on the total angular momentum and Stevens coefficients [67,68], and $d_l^{0m}(\theta)$ is related to the associated Legendre polynomials, which with $e^{im\phi}$ can be expressed in terms of the complex spherical harmonics [69].

Equation (1) has been used to calculate the single-ion anisotropy at all the R sites in the interface, using $\mathcal{A}_l$ values appropriate for Sm. Figure 7 presents the results for sites

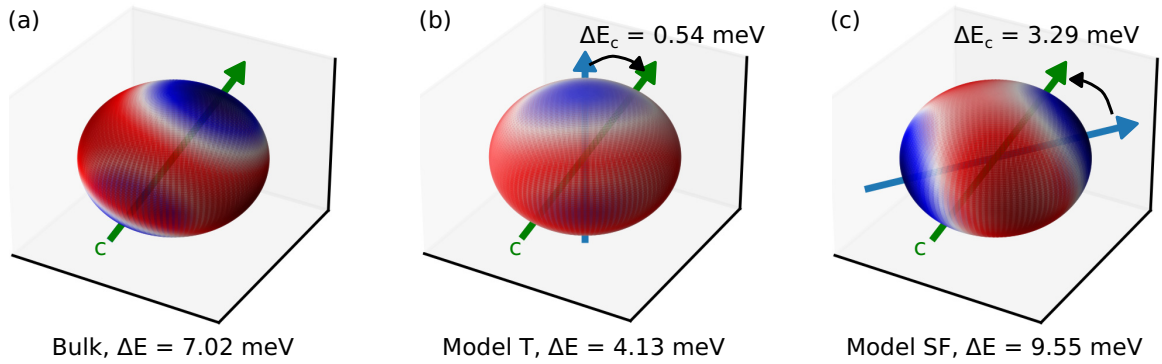


FIG. 7. Energy as a function of moment orientation calculated using Eq. (1) for bulk $SmFe_{12}$ or for the Sm site closest to the interface plane in the two models. In the color maps, blue and red correspond to the easiest and hardest directions, respectively. The blue and green arrows denote the local easy direction and c axis, respectively (only one of the two possible c axes is shown for model T). ΔE and ΔE_c are defined in the text.

located closest to the interface plane in each model, and also for bulk $SmFe_{12}$. At each site, one can find the local easy direction which minimizes E, and also define a local anisotropy energy ΔE as the difference between the maximum and minimum of E. It is also useful to introduce the quantity ΔE_c, which is the energy cost of rotating the moment from its local easy direction to the direction parallel to the c axis.

In bulk [Fig. 7(a)], the easy direction coincides with the c axis and there is a large ΔE value of 7.02 meV (this value reduces if Ti is present at neighboring 8i sites [59]). In the interface models, R sites at a distance greater than 4 Å from the interface plane have similarly large values of ΔE. These values are shown as symbols in Fig. 6, which shows how the variations in ΔE for these sites follow the variations in $-A_{20}\langle r^2\rangle$. Three of these four sites also have easy directions along the c axis, but the site in model SF located 5.1 Å from the interface has an easy direction which is rotated by 5° with respect to c.

The R sites closest to the interface planes show much stronger variations in ΔE and have substantial differences in the easy direction. For model T, based on its symmetry, the easy direction of the R site within the interface plane should either point perpendicular or parallel to this plane. The calculated anisotropy energy [Fig. 7(b)] confirms this and shows that the easy axis is perpendicular to the interface plane, pointing exactly halfway between the c axes of the twinned regions [$29^\circ = \tan^{-1}(c/a)$ with respect to c]. This direction can equivalently be seen as the average of the two grains' easy directions. Furthermore, at this site, ΔE is reduced to 4.13 meV, and the energy cost ΔE_c of rotating the moment from this easy direction to c is only 0.54 meV.

In model SF [Fig. 7(c)], the difference from bulk is dramatic. The ΔE value of 9.55 meV is larger than in bulk, and the easy direction is strongly misaligned from c, at an angle of 49°. ΔE_c is also substantial, i.e., 3.29 meV. The behavior of this site shows the importance of considering all CF coefficients, not just $A_{20}\langle r^2\rangle$; looking only at this number (bars in Fig. 6) might have led to the conclusion that the anisotropy at this site was weak. It is also interesting to note the anisotropy in the plane perpendicular to the easy direction, evident from the color map in Fig. 7(c). The RDFs in Fig. 4 help explain the different single-ion anisotropy of this site. The local environment (closer than 4 Å, previously found to be a critical radius for affecting CF coefficients [59]) is substantially different compared to bulk, with a new R site and reduced Fe coordination. Given their +3 charge state, the R ions' positions are likely to be particularly important in determining the orientation of Sm's prolate 4f electron cloud.

Figure 8 summarizes the calculations of the single-ion anisotropy, showing the easy axes at the different sites explored in the calculations. All of the easy axes lie parallel to the (010) plane. These diagrams emphasize how the additional RT_4 plane in model SF causes a major disruption in anisotropy, creating a region approximately 2 Å wide where the easy direction is 49° to the c axis, and a wider region (approximately 10 Å) where the influence is much weaker, but still noticeable as a small change in the easy direction. By contrast, the mirror plane in model T shows relatively simple behavior, with an easy axis which is an average of the c axes of the two regions. It should be noted that this direction would also correspond to the global easy axis of a crystal composed of two identical grains twinned in this way, since this is determined by the same average.

IV. CONCLUSIONS AND OUTLOOK

Recently published HAADF-STEM images have been used to derive atomistic models of the two reported twinning

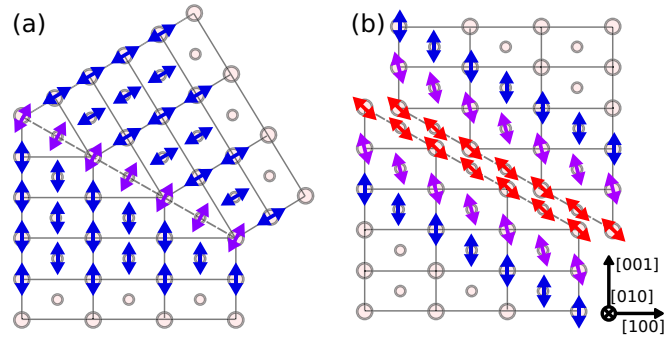


FIG. 8. Schematic representation (see, also, Fig. 2) of the local easy axes at different R sites in (a) model T and (b) model SF. All easy axes lie in the plane of the page (010). The blue arrows are parallel to the c axis.

structures. One structure is a simple reflection in a {101} plane, which has no effect on the stoichiometry. The *R* atoms at this interface have essentially identical RDFs to bulk RT_{12}. The other structure involves the insertion of an RT_4 plane followed by an offset of $a/2$ in the [100] direction (loosely described as a stacking fault) followed by a reflection. This structure is *R*-rich and the RDFs show large differences compared to bulk. Two periodically repeating models have been constructed, model T and model SF, to investigate the reflection and the stacking fault, respectively, and their properties have been calculated using first-principles DFT. Analysis both of magnetic moments and crystal field coefficients finds that only the atoms within ∼4 Å of the interface plane are strongly affected by the reflection or stacking fault. In model T, the *R* atoms in the reflection plane show a weakened single-ion anisotropy and have an easy direction equal to the average of the *c* axes of the two grains. However, in model SF, the *R* atoms closest to the interface have an enhanced single-ion anisotropy compared to bulk, with an easy direction 49° to the *c* axis. The effects on the next-closest *R* atoms are much smaller, but the easy direction is slightly rotated away from *c*.

This work has addressed the first key question in Sec. I and quantified the effect of experimentally observed extended defect structures on the microscopic anisotropy. The "stacking fault" does indeed induce substantial changes in single-ion anisotropy, but only in the atoms closest to the interface. The pressing issue now is to address the second key question and understand what effect these microscopic changes have on the macroscopic phenomena of magnetization reversal and coercivity. Although micromagnetics calculations may provide some indication, we note that the small length scale (2 Å) may not be well described by a continuum approximation. Atomistic spin dynamics calculations do not make this approximation and have been used to study magnetization and domain-wall structure in $Nd_2Fe_{14}B$ [35,70,71]. Therefore, the likely next step is to use the calculated results as input for ASD simulations.

As noted in Sec. II, this study has focused on the simplest (and thermodynamically unstable) RFe_{12} composition and has not attempted to investigate substitutions of Co, Ti, or V. In bulk, there is a strong tendency for Ti or V atoms to occupy 8*i* sites, and as noted above, the RT_4 plane contains two 8*i* sites. On the other hand, while the STEM-EDS measurements in Ref. [26] are not conclusive, there is some evidence for a depletion of Ti in the interface region [26]. It will be important to investigate the site preference energetics of substitutional *T* atoms in these interface structures, and also to confirm that their effects on the crystal field are in line with those predicted by a point charge model [59]. More generally, first-principles calculations should be used to address the key question of understanding the relative stability of the different types of interfaces. If these different interfaces do indeed affect the coercivity, determining the conditions which promote the formation of one over the other would be a major step forward in controlling the performance of practical one-twelve magnets. Finally, both MM and ASD require knowledge of the exchange interactions. Based on the relatively small changes in magnetic moments that were calculated for the interface models, it is likely that bulk calculations could be used to parametrize the exchange interactions, as a first approximation. However, a first-principles calculation of exchange coupling in the interface models introduced here would test the validity of this approximation and also provide further fundamental insight into the nature of exchange across interfaces.

ACKNOWLEDGMENTS

I am grateful for computational support from the UK national high performance computing service, ARCHER2, for which access was obtained via the UKCP consortium and funded by Engineering and Physical Sciences Research Council Grant No. EP/X035891/1. I thank J. B. Staunton for a critical reading of the manuscript. I also thank A. Bolyachkin and H. Sepehri-Amin for helpful discussions about the data of Ref. [26], and A. Gabay, G. Hadjipanayis, and L. H. Lewis for initial discussions about one-twelve magnets.

DATA AVAILABILITY

The data that support the findings of this article are not publicly available upon publication because it is not technically feasible and/or the cost of preparing, depositing, and hosting the data would be prohibitive within the terms of this research project. The data are available from the authors upon reasonable request.

[1] P. Tozman, H. Sepehri-Amin, and K. Hono, Prospects for the development of $SmFe_{12}$-based permanent magnets with a $ThMn_{12}$-type phase, Scr. Mater. **194**, 113686 (2021).

[2] A. Gabay and G. Hadjipanayis, Recent developments in RFe_{12}-type compounds for permanent magnets, Scr. Mater. **154**, 284 (2018).

[3] Y. Hirayama, Y. Takahashi, S. Hirosawa, and K. Hono, Intrinsic hard magnetic properties of $Sm(Fe_{1-x}Co_x)_{12}$ compound with the $ThMn_{12}$ structure, Scr. Mater. **138**, 62 (2017).

[4] K. Buschow, Permanent magnet materials based on tetragonal rare earth compounds of the type $RFe_{12-x}M_x$, J. Magn. Magn. Mater. **100**, 79 (1991).

[5] A. Schönhöbel, R. Madugundo, O. Y. Vekilova, O. Eriksson, H. Herper, J. Barandiarán, and G. Hadjipanayis, Intrinsic magnetic properties of $SmFe_{12-x}V_x$ alloys with reduced V-concentration, J. Alloys Compd. **786**, 969 (2019).

[6] H. Makuta, H. Machida, and T. Fujiwara, Coercivity and microstructure dependence on B content in $ThMn_{12}$-type Sm-Zr-Fe-Co-Ti-Cu-B alloys, Mater. Trans. **66**, 254 (2025).

[7] Y. Xu and G. C. Hadjipanayis, Intrinsic and hard magnetic properties of $(Sm_{1-x}R_x)$-Fe-Co-V alloys (R = Gd, Zr, and Y), J. Magn. Magn. Mater. **603**, 172236 (2024).

[8] P. Tozman, T. Fukazawa, D. Ogawa, H. Sepehri-Amin, A. Bolyachkin, T. Miyake, S. Hirosawa, K. Hono, and Y. Takahashi, Peculiar behavior of V on the Curie temperature and anisotropy field of $SmFe_{12-x}V_x$ compounds, Acta Mater. **232**, 117928 (2022).

[9] Y. Harashima, T. Fukazawa, H. Kino, and T. Miyake, Effect of R-site substitution and the pressure on stability of $R\mathrm{Fe}_{12}$: A first-principles study, J. Appl. Phys. **124**, 163902 (2018).

[10] T. Kuno, S. Suzuki, K. Urushibata, K. Kobayashi, N. Sakuma, M. Yano, A. Kato, and A. Manabe, $(\mathrm{Sm,Zr})(\mathrm{Fe,Co})_{11.0-11.5}\mathrm{Ti}_{1.0-0.5}$ compounds as new permanent magnet materials, AIP Adv. **6**, 025221 (2016).

[11] T. Fukazawa, Y. Harashima, and T. Miyake, First-principles study on the stability of $(R,\mathrm{Zr})(\mathrm{Fe,Co,Ti})_{12}$ against 2-17 and unary phases (R=Y, Nd, Sm), Phys. Rev. Mater. **6**, 054404 (2022).

[12] S. Kobayashi, D. Ogawa, X. Xu, Y. Takahashi, A. Martin-Cid, K. Ishigami, Y. Kotani, M. Suzuki, T. Yoshioka, H. Tsuchiura, H. Sepehri-Amin, T. Ohkubo, K. Hono, S. Hirosawa, and T. Nakamura, Multimodal analysis of Zr substitution effects on magnetic and crystallographic properties in $(\mathrm{Sm}_{1-x}\mathrm{Zr}_x)(\mathrm{Fe}_{0.8}\mathrm{Co}_{0.2})_{12}$ compounds with ThMn_{12} structure, Acta Mater. **242**, 118454 (2023).

[13] M. Matsumoto, T. Hawai, and K. Ono, $(\mathrm{Sm,Zr})\mathrm{Fe}_{12-x}M_x$ (M = Zr, Ti, Co) for permanent-magnet applications: *ab initio* material design integrated with experimental characterization, Phys. Rev. Appl. **13**, 064028 (2020).

[14] Y. Harashima, K. Terakura, H. Kino, S. Ishibashi, and T. Miyake, Nitrogen as the best interstitial dopant among X = B, C, N, O, and F for strong permanent magnet $\mathrm{NdFe}_{11}\mathrm{Ti}X$: First-principles study, Phys. Rev. B **92**, 184426 (2015).

[15] A. H. Tkaczyk, A. Bartl, A. Amato, V. Lapkovskis, and M. Petranikova, Sustainability evaluation of essential critical raw materials: Cobalt, niobium, tungsten and rare earth elements, J. Phys. D: Appl. Phys. **51**, 203001 (2018).

[16] D. Palanisamy, S. Ener, F. Maccari, L. Schäfer, K. P. Skokov, O. Gutfleisch, D. Raabe, and B. Gault, Grain boundary segregation, phase formation, and their influence on the coercivity of rapidly solidified $\mathrm{SmFe}_{11}\mathrm{Ti}$ hard magnetic alloys, Phys. Rev. Mater. **4**, 054404 (2020).

[17] G. Hadjipanayis, A. Gabay, A. Schönhöbel, A. Martán-Cid, J. Barandiaran, and D. Niarchos, ThMn_{12}-Type alloys for permanent magnets, Engineering **6**, 141 (2020).

[18] H. Sepehri-Amin, Y. Tamazawa, M. Kambayashi, G. Saito, Y. Takahashi, D. Ogawa, T. Ohkubo, S. Hirosawa, M. Doi, T. Shima, and K. Hono, Achievement of high coercivity in $\mathrm{Sm}(\mathrm{Fe}_{0.8}\mathrm{Co}_{0.2})_{12}$ anisotropic magnetic thin film by boron doping, Acta Mater. **194**, 337 (2020).

[19] J. S. Zhang, X. Tang, H. Sepehri-Amin, A. K. Srinithi, T. Ohkubo, and K. Hono, Origin of coercivity in an anisotropic $\mathrm{Sm(Fe,Ti,V)}_{12}$-based sintered magnet, Acta Mater. **217**, 117161 (2021).

[20] A. Gabay, C. Han, C. Ni, and G. Hadjipanayis, Effect of alloying with Sc, Nb and Zr on reduction-diffusion synthesis of magnetically hard $\mathrm{Sm(Fe,Co,Ti)}_{12}$-based monocrystalline powders, J. Magn. Magn. Mater. **541**, 168550 (2022).

[21] A. Bolyachkin, H. Sepehri-Amin, M. Kambayashi, Y. Mori, T. Ohkubo, Y. Takahashi, T. Shima, and K. Hono, Coercivity engineering in $\mathrm{Sm}(\mathrm{Fe}_{0.8}\mathrm{Co}_{0.2})_{12}\mathrm{B}_{0.5}$ thin films by Si grain boundary diffusion, Acta Mater. **227**, 117716 (2022).

[22] N. Polin, A. M. Gabay, C. Han, C. Chan, S.-H. Kim, C. Ni, O. Gutfleisch, G. C. Hadjipanayis, and B. Gault, Understanding high coercivity in ThMn_{12}-type Sm–Zr–Fe–Co–Ti permanent magnet powders through nanoscale analysis, Scr. Mater. **259**, 116537 (2025).

[23] J. Zhang, X. Tang, A. Bolyachkin, A. Srinithi, T. Ohkubo, H. Sepehri-Amin, and K. Hono, Microstructure and extrinsic magnetic properties of anisotropic $\mathrm{Sm(Fe,Ti,V)}_{12}$-based sintered magnets, Acta Mater. **238**, 118228 (2022).

[24] S. Ener, K. P. Skokov, D. Palanisamy, T. Devillers, J. Fischbacher, G. G. Eslava, F. Maccari, L. Schäfer, L. V. Diop, I. Radulov, B. Gault, G. Hrkac, N. M. Dempsey, T. Schrefl, D. Raabe, and O. Gutfleisch, Twins – A weak link in the magnetic hardening of ThMn_{12}-type permanent magnets, Acta Mater. **214**, 116968 (2021).

[25] I. Dirba, J. Li, H. Sepehri-Amin, T. Ohkubo, T. Schrefl, and K. Hono, Anisotropic, single-crystalline SmFe_{12}-based microparticles with high roundness fabricated by jet-milling, J. Alloys Compd. **804**, 155 (2019).

[26] P. Tozman, G. Hrkac, C. Patrick, J. Staunton, T. Saito, T. Sasaki, T. Ohkubo, and H. Sepehri-Amin, Effect of Co on twin formation and magnetic properties of $\mathrm{Sm(Fe,Ti,V)}_{12}$ alloys, Scr. Mater. **258**, 116491 (2025).

[27] K. H. J. Buschow, Intermetallic compounds of rare-earth and 3D transition metals, Rep. Prog. Phys. **40**, 1179 (1977).

[28] H. Moriya, H. Tsuchiura, and A. Sakuma, First principles calculation of crystal field parameter near surfaces of $\mathrm{Nd}_2\mathrm{Fe}_{14}\mathrm{B}$, J. Appl. Phys. **105**, 07A740 (2009).

[29] N. Umetsu, A. Sakuma, and Y. Toga, First-principles study of interface magnetic structure in $\mathrm{Nd}_2\mathrm{Fe}_{14}\mathrm{B}/(\mathrm{Fe,Co})$ exchange spring magnets, Phys. Rev. B **93**, 014408 (2016).

[30] H. Kronmüller, Theory of nucleation fields in inhomogeneous ferromagnets, Phys. Stat. Sol. (b) **144**, 385 (1987).

[31] H Kronmüller and D. Goll, Micromagnetic theory of the pinning of domain walls at phase boundaries, Phys. B: Condens. Matter **319**, 122 (2002).

[32] J. Fischbacher, A. Kovacs, M. Gusenbauer, H. Oezelt, L. Exl, S. Bance, and T. Schrefl, Micromagnetics of rare-earth efficient permanent magnets, J. Phys. D: Appl. Phys. **51**, 193002 (2018).

[33] R. F. L. Evans, Atomistic spin dynamics, in *Handbook of Materials Modeling: Applications: Current and Emerging Materials*, edited by W. Andreoni and S. Yip (Springer, Cham, 2018), pp. 1–23.

[34] M. Nishino, Y. Toga, S. Miyashita, H. Akai, A. Sakuma, and S. Hirosawa, Atomistic-model study of temperature-dependent domain walls in the neodymium permanent magnet $\mathrm{Nd}_2\mathrm{Fe}_{14}\mathrm{B}$, Phys. Rev. B **95**, 094429 (2017).

[35] Q. Gong, M. Yi, R. F. L. Evans, B.-X. Xu, and O. Gutfleisch, Calculating temperature-dependent properties of $\mathrm{Nd}_2\mathrm{Fe}_{14}\mathrm{B}$ permanent magnets by atomistic spin model simulations, Phys. Rev. B **99**, 214409 (2019).

[36] H. Sepehri-Amin, J. Thielsch, J. Fischbacher, T. Ohkubo, T. Schrefl, O. Gutfleisch, and K. Hono, Correlation of microchemistry of cell boundary phase and interface structure to the coercivity of $\mathrm{Sm}(\mathrm{Co}_{0.784}\mathrm{Fe}_{0.100}\mathrm{Cu}_{0.088}\mathrm{Zr}_{0.028})_{7.19}$ sintered magnets, Acta Mater. **126**, 1 (2017).

[37] A. Bolyachkin, E. Dengina, N. Kulesh, X. Tang, H. Sepehri-Amin, T. Ohkubo, and K. Hono, Tomography-based digital twin of Nd-Fe-B permanent magnets, npj Comput. Mater. **10**, 34 (2024).

[38] S. C. Westmoreland, C. Skelland, T. Shoji, M. Yano, A. Kato, M. Ito, G. Hrkac, T. Schrefl, R. F. L. Evans, and R. W. Chantrell, Atomistic simulations of $\alpha-\mathrm{Fe}/\mathrm{Nd_2Fe_{14}B}$ magnetic core/shell nanocomposites with enhanced energy product for high temperature permanent magnet applications, J. Appl. Phys. **127**, 133901 (2020).

[39] J. Fischbacher, A. Kovacs, H. Oezelt, M. Gusenbauer, T. Schrefl, L. Exl, D. Givord, N. M. Dempsey, G. Zimanyi, M. Winklhofer, G. Hrkac, R. Chantrell, N. Sakuma, M. Yano, A. Kato, T. Shoji, and A. Manabe, On the limits of coercivity in permanent magnets, Appl. Phys. Lett. **111**, 072404 (2017).

[40] P. Hohenberg and W. Kohn, Inhomogeneous electron gas, Phys. Rev. **136**, B864 (1964).

[41] W. Kohn and L. J. Sham, Self-consistent equations including exchange and correlation effects, Phys. Rev. **140**, A1133 (1965).

[42] M. Richter, Band structure theory of magnetism in $3d$-$4f$ compounds, J. Phys. D: Appl. Phys. **31**, 1017 (1998).

[43] M. S. S. Brooks, L. Nordstrom, and B. Johansson, $3d$-$5d$ band magnetism in rare earth-transition metal intermetallics: Total and partial magnetic moments of the $R\mathrm{Fe_2}(R = \mathrm{Gd} - \mathrm{Yb})$ Laves phase compounds, J. Phys.: Condens. Matter **3**, 2357 (1991).

[44] T. Fukazawa, H. Akai, Y. Harashima, and T. Miyake, First-principles investigation of $\mathrm{Nd(Fe}, M)_{12} (M = \mathrm{K} - \mathrm{Br})$ and $\mathrm{Nd(Fe, Cr, Co, Ni, Ge, As)_{12}}$: Possible enhancers of Curie temperature for $\mathrm{NdFe_{12}}$ magnetic compounds, Acta Mater. **226**, 117597 (2022).

[45] H. C. Herper, K. P. Skokov, S. Ener, P. Thunström, L. V. Diop, O. Gutfleisch, and O. Eriksson, Magnetic properties of $\mathrm{NdFe_{11}Ti}$ and $\mathrm{YFe_{11}Ti}$, from experiment and theory, Acta Mater. **242**, 118473 (2023).

[46] T. Yoshioka, H. Tsuchiura, and P. Novák, Effect of element doping and substitution on the electronic structure and macroscopic magnetic properties of $\mathrm{SmFe_{12}}$-based compounds, Phys. Rev. B **105**, 014402 (2022).

[47] P. Larson, I. I. Mazin, and D. A. Papaconstantopoulos, Effects of doping on the magnetic anisotropy energy in $\mathrm{SmCo_{5-x}Fe_x}$ and $\mathrm{YCo_{5-x}Fe_x}$, Phys. Rev. B **69**, 134408 (2004).

[48] C. E. Patrick and J. B. Staunton, Rare-earth/transition-metal magnets at finite temperature: Self-interaction-corrected relativistic density functional theory in the disordered local moment picture, Phys. Rev. B **97**, 224415 (2018).

[49] P. Delange, S. Biermann, T. Miyake, and L. Pourovskii, Crystal-field splittings in rare-earth-based hard magnets: An *ab initio* approach, Phys. Rev. B **96**, 155132 (2017).

[50] C. E. Patrick and J. B. Staunton, Crystal field coefficients for yttrium analogues of rare-earth/transition-metal magnets using density-functional theory in the projector-augmented wave formalism, J. Phys.: Condens. Matter **31**, 305901 (2019).

[51] J. Bouaziz, C. E. Patrick, and J. B. Staunton, Crucial role of Fe in determining the hard magnetic properties of $\mathrm{Nd_2Fe_{14}B}$, Phys. Rev. B **107**, L020401 (2023).

[52] S. Hirosawa, Y. Matsuura, H. Yamamoto, S. Fujimura, M. Sagawa, and H. Yamauchi, Magnetization and magnetic anisotropy of $\mathrm{R_2Fe_{14}B}$ measured on single crystals, J. Appl. Phys. **59**, 873 (1986).

[53] A. Ermolenko, Exchange interactions and magnetocrystalline anisotropy of rare earth - cobalt compounds with $\mathrm{CaCu_5}$-type structure, IEEE Trans. Magn. **15**, 1765 (1979).

[54] O. Moze, L. Pareti, M. Solzi, and W. David, Neutron diffraction and magnetic anisotropy study of Y-Fe-Ti intermetallic compounds, Solid State Commun. **66**, 465 (1988).

[55] J. Ihm, A. Zunger, and M. L. Cohen, Momentum-space formalism for the total energy of solids, J. Phys. C: Solid State Phys. **12**, 4409 (1979).

[56] It should be noted that "stacking fault" is a convenient label which captures the offset columns of rare-earth atoms, but the structure is not a conventional stacking fault due to the insertion of extra planes of atoms.

[57] See Supplemental Material at http://link.aps.org/supplemental/10.1103/syc2-qzdf for structure files of the interface models.

[58] L. V. Pourovskii, J. Boust, R. Ballou, G. G. Eslava, and D. Givord, Higher-order crystal field and rare-earth magnetism in rare-earth–$\mathrm{Co_5}$ intermetallics, Phys. Rev. B **101**, 214433 (2020).

[59] C. E. Patrick, Y. Huang, L. H. Lewis, and J. B. Staunton, Theory of defect-induced crystal field perturbations in rare-earth magnets, Phys. Rev. Lett. **132**, 056703 (2024).

[60] Y. Harashima, K. Terakura, H. Kino, S. Ishibashi, and T. Miyake, First-principles study of structural and magnetic properties of $R\mathrm{(Fe, Ti)_{12}}$ and $R\mathrm{(Fe, Ti)_{12}N} (R = \mathrm{Nd, Sm, Y})$, JPS Conf. Proc. **5**, 011021 (2015).

[61] J. P. Perdew and Y. Wang, Accurate and simple analytic representation of the electron-gas correlation energy, Phys. Rev. B **45**, 13244 (1992).

[62] P. E. Blöchl, Projector augmented-wave method, Phys. Rev. B **50**, 17953 (1994).

[63] J. Enkovaara, C. Rostgaard, J. J. Mortensen, J. Chen, M. Dułak, L. Ferrighi, J. Gavnholt, C. Glinsvad, V. Haikola, H. A. Hansen, H. H. Kristoffersen, M. Kuisma, A. H. Larsen, L. Lehtovaara, M. Ljungberg, O. Lopez-Acevedo, P. G. Moses, J. Ojanen, T. Olsen, V. Petzold, N. A. Romero, J. Stausholm-Møller, M. Strange, G. A. Tritsaris, M. Vanin, M. Walter, B. Hammer, H. Häkkinen, G. K. H. Madsen, R. M. Nieminen, J. K. Nørskov, M. Puska, T. T. Rantala, J. Schiøtz, K. S. Thygesen, and K. W. Jacobsen, Electronic structure calculations with GPAW: A real-space implementation of the projector augmented-wave method, J. Phys.: Condens. Matter **22**, 253202 (2010).

[64] M. Lüders, A. Ernst, M. Däne, Z. Szotek, A. Svane, D. Ködderitzsch, W. Hergert, B. L. Györffy, and W. M. Temmerman, Self-interaction correction in multiple scattering theory, Phys. Rev. B **71**, 205109 (2005).

[65] D. J. Newman and B. Ng, The superposition model of crystal fields, Rep. Prog. Phys. **52**, 699 (1989).

[66] M. D. Kuz'min and A. M. Tishin, Theory of crystal-field effects in $3d$-$4f$ intermetallic compounds, in *Handbook of Magnetic Materials*, edited by K. H. J. Buschow, Vol. 17 (Elsevier, Amsterdam, 2008), Chap. 3, p. 149.

[67] K. W. H. Stevens, Matrix elements and operator equivalents connected with the magnetic properties of rare earth ions, Proc. Phys. Soc. A **65**, 209 (1952).

[68] J. Sievers, Asphericity of $4f$-shells in their Hund's rule ground states, Z. Phys. B **45**, 289 (1982).

[69] A. R. Edmonds, *Angular Momentum in Quantum Mechanics* (Princeton University Press, Princeton, NJ, 1960), Chap. 4, p. 59.

[70] Y. Toga, M. Nishino, S. Miyashita, T. Miyake, and A. Sakuma, Anisotropy of exchange stiffness based on atomic-scale magnetic properties in the rare-earth permanent magnet $Nd_2Fe_{14}B$, Phys. Rev. B **98**, 054418 (2018).

[71] M. Nishino, I. E. Uysal, and S. Miyashita, Effect of the surface magnetic anisotropy of neodymium atoms on the coercivity in neodymium permanent magnets, Phys. Rev. B **103**, 014418 (2021).